# Dynamics of Nematic MBBA Film Induced by Transient Grating under a Strong Absorption Condition

**Bohyun Yoon, Sun Hee Kim, Ilkeun Lee, and Seong Kyu Kim\***

*Department of Chemistry and Basic Science Research Institute, Sungkyunkwan University, Suwon, 440-746, Korea*

**Minhaeng Cho**

*Department of Chemistry, Korea University, Seoul, 136-701, Korea*

**Hackjin Kim**

*Department of Chemistry, Chungnam National University, Taejon, 305-764, Korea*

*Received: February 24, 1998; In Final Form: June 4, 1998*

We report time profiles of transient grating diffraction signals created by crossed beam excitation of 170 $\mu$m thick nematic MBBA film. At the excitation wavelength of 355 nm and the irradiance of 10 mJ/cm$^2$, corresponding to a strong absorption condition, the signal consists of four distinguishable components in the time range of submicroseconds to milliseconds. When the grating spacing is 8 $\mu$m, the fastest component due to thermal diffusion near the surface rises within the time resolution of the experiments ($\sim$20 ns) and decays in about 10 $\mu$s. This component exhibits a strong dependence on the polarization of the probe beam, which reduces as the temperature approaches the nematic–isotropic phase transition point. The weakest and slowest component observed in the time scale of 100 ms is identified as mass diffusion of *cis*-MBBA. The other two components of the diffraction signal dominant in the submillisecond and the millisecond regimes, respectively, display an exponential rise followed by an exponential decay. These components are interpreted as dynamics of the reordering processes induced by temperature perturbation and by the phototransformed state, respectively. As the temperature approaches the phase transition point, the optical nonlinearity increases to such an extent that multiple order diffractions are visible. The phototransformed state, with a significant contribution from laser-induced melting, is the major cause of the extraordinarily high optical nonlinearlity of MBBA near the phase transition point.

## Introduction

Because of the high tendency for alignment, liquid crystals show very interesting physical properties;[1–3] their flowing, thermal, mechanical, optical, and electrical properties are highly anisotropic. Some of these properties have been taken advantage of in developing electrooptical devices. Liquid crystals also possess largely nonlinear optical properties. The nonlinear optical effects represent the material's ability to produce new polarization under an external optical field. In solid materials, the high optical nonlinearity can be induced by electronic redistribution under the external field through various processes such as the optical Kerr effect or electrostrictive interaction. In liquids, nuclear reorientation as well as electronic redistribution is possible through the optical Kerr effect. However, because of weak molecular interaction in liquids, the newly created molecular polarization is weak and relaxes ultrafast. In liquid crystals, the intermolecular interaction is weak enough for individual molecules to respond to the external field and strong enough to produce additive polarization. The large nonlinear optical effects of liquid crystals are thus induced significantly by the collective molecular motions on much slower time scales.

The nonlinear optical properties can be investigated by numerous techniques such as self-focusing, optical phase conjugation, four wave mixing, and so on. When more fundamental light–matter interactions are to be investigated, the conventional nonlinear optical techniques can adopt additional features such as time or frequency resolution. The transient grating (TG) method that we have used in this work is a time-resolved version of the general four wave mixing technique. In our TG method, two replica nanosecond laser pulses are crossed at the sample to induce a sinusoidal excitation pattern with fringe spacing $\Lambda$ and the sample response is read by the diffraction of a CW He/Ne laser beam. The diffraction signal is proportional to the sum of the squares of changes in the phase refractive index ($\Delta n$) and in the extinction coefficient ($\Delta k$), that is,

$$I(t) \propto (\Delta n)^2 + (\Delta k)^2 \qquad (1)$$

where $\Delta$ denotes the difference between the peak and the null of the grating.

In this work we have studied MBBA (4-methoxybenzylidene-4-*n*-butylaniline), which is one of the most studied liquid crystals. Yet, from a viewpoint of fundamental light–matter interaction in the nonlinear optical dynamics, even this most studied liquid crystal has left many unresolved questions. MBBA forms a nematic phase between 21 °C (solid → nematic, $T_{sn}$) and 46.5 °C (nematic → isotropic, $T_{ni}$). The alignment of liquid crystals is described by the order parameter $S$, which is

* To whom correspondence should be addressed. Tel: 82-331-290-7069. Fax: 82-331-290-7075. E-mail: skkim@chem.skku.ac.kr.
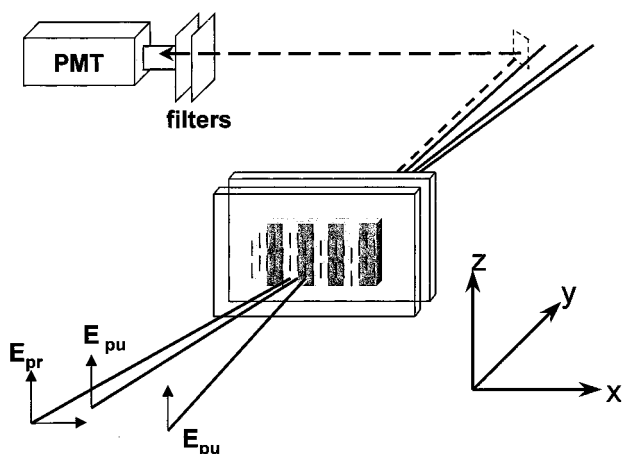
**Figure 1.** Directions of the excitation fields ($\mathbf{E}_{pu}$), the probe field ($\mathbf{E}_{pr}$), and the sample alignment.

defined as $\langle (3\cos^2\theta - 1)/2 \rangle$, where $\theta$ is the angle between the molecular axis and the director axis and $\langle ... \rangle$ denotes the average over all molecular orientations. $S$ is a strong function of temperature, varying between about 0.6 near $T_{sn}$ and about 0.2 near $T_{ni}$ for most nematic liquid crystals. Molecularly, MBBA exists in the trans form with respect to the $-CH=N-$ bond but undergoes the trans $\rightarrow$ cis photoisomerization at the excitation wavelength (355 nm) of this work. The appearance of the photoisomer disturbs the alignment of nematic *trans*-MBBA and induces a large nonlinear optical effects.[4] The recovery time of *trans*-MBBA has been reported to be between 0.15 and 1.6 s at the nematic temperatures.[4-6] Since *trans*- and *cis*-MBBA are transparent at the probe wavelength (633 nm), only the $\Delta n$ term dominates the signal.

By employment of the dynamic grating methods, various nematic liquid crystal films[4-12] including MBBA have been studied. Heat induced flow, diffusion, acoustic wave propagation, and the director axis reorientation are suggested to explain the observed dynamics depending on the experimental conditions. For nematic MBBA, the mass diffusion and the thermal diffusion have been studied using the TG method.[6,11,12] Most of these experiments have been done using very low power density of the excitation or excitation wavelength outside the absorption region. Occasionally and especially under the strong absorption conditions of laser power and wavelength, development of strong and slow components accompanying unusually strong multiple order diffractions have been observed. Accordingly, the nonlinear optical property increases substantially under the strong absorption condition. In this work, we have studied the dynamics of nonlinear optical processes of nematic MBBA under strong absorption conditions.

**Experimental Section**

The optical layout and other details of our TG setup are found elsewhere.[13,14] Here we present Figure 1 to show the directions of the optical fields and the sample alignment. We prepared planar homogeneously aligned MBBA (Tokyo Kasei, used as received) sandwiched between a pair of indium tin oxide glasses spaced by a 170 $\mu$m thick Teflon sheet. The alignment is achieved by rubbing the glasses unidirectionally. The sample is then placed, with the preferential director axis along the $z$-axis in Figure 1, inside a metal block that is temperature controlled within $\pm 0.1$ °C. For the sinusoidal (along $x$-axis) excitation, two replica pulses of 355 nm from a Q-switched Nd:YAG laser are recombined at the sample. The overlap beam diameter is 3.8 mm, and the irradiance of the excitation is about 10 mJ/
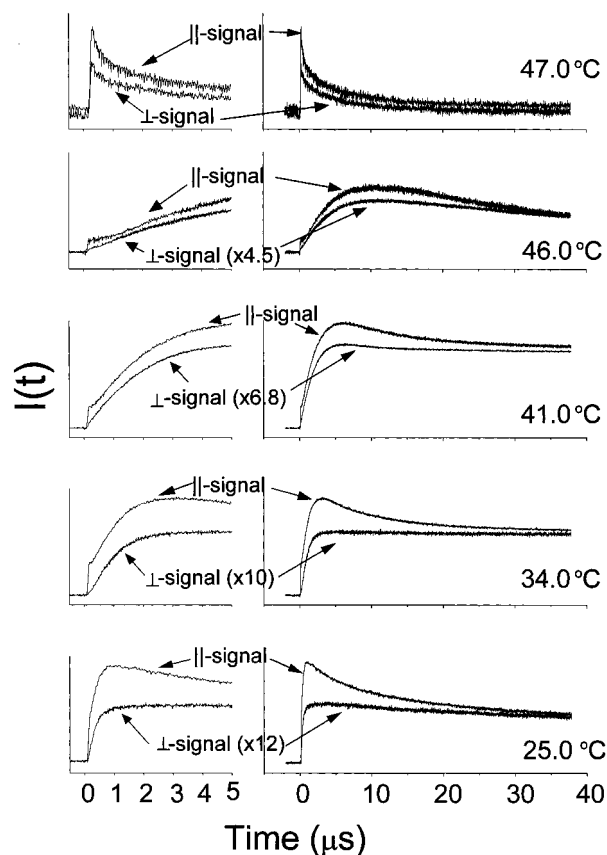


**Figure 2.** Diffraction signals in the short time region. The fringe spacing ($\Lambda$) is 8.0 $\mu$m. At nematic temperatures, the $\perp$-signals are much weaker than the corresponding $\parallel$-signals and are thus multiplied by the number shown in each parenthesis to match the tailing backgrounds. The rise parts of the signals are shown in the faster time windows on the left. The signals from the isotropic sample at 47.0 °C are smaller by nearly 3 orders of magnitude than those at nematic temperatures, and the anisotropic diffraction efficiency disappears. The $\perp$-signal at 47.0 °C is shown downshifted to distinguish it from the $\parallel$-signal.

cm$^2$. The fringe spacing is varied between 2 and 12 $\mu$m by changing the crossing angle of the excitation pulses. The electric field of the excitation is polarized parallel to the director axis. The CW probe from a 2 mW He/Ne laser (633 nm) whose polarization is switchable is then introduced at the Bragg angle. The first order diffraction at all temperatures and the multiple order diffractions at high nematic temperatures can be seen by the naked eye. Details of the multiple order diffractions are not discussed here. The PMT output by the transient diffraction is read with a transient digitizer and averaged mathematically for 100 laser shots at the repetition rate of 1 Hz or less. The background signal is also obtained by blocking one of the excitation beams and then subtracted from the transient signal.

Freshness and alignment of the sample are critical for reproducible data acquisition. Only well-aligned fresh samples gave the diffraction signal with a large anisotropic dependence on the probe polarization and with the sharp break of the diffraction intensity at $T_{ni}$. The fresh samples that were exposed to less than 1000 shots were used in the experiments.

**Results**

In Figure 2, the first order TG diffraction signals ($I(t)$) in the microsecond time scale are shown at various temperatures. The fringe spacing for these signals is 8.0 $\mu$m. At the nematic temperatures, a large difference in the diffraction signals depending on the polarization of the probe beam is observed.
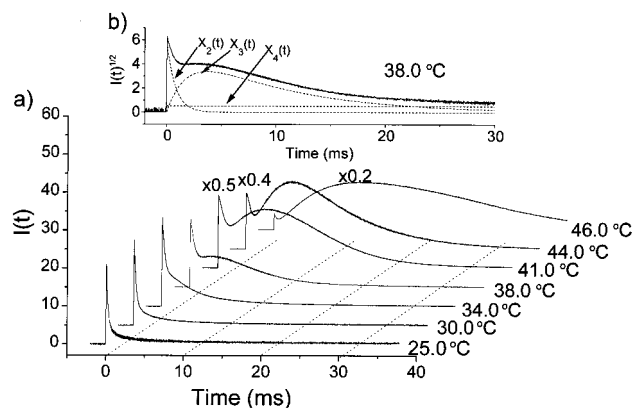
**Figure 3.** (a) Diffraction signals in the long time region. The fringe spacing ($\Lambda$) is 8.0 $\mu$m. Only the ∥-signals are shown. (b) Root of the ∥-signal at 38.0 °C with the fit components (dashed curves, $X_2(t)$, $X_3(t)$, $X_4(t)$). The sum of the fit components is indistinguishable from the signal and is omitted. The ordinates are in arbitrary experimental scale.

Overall, the probe beam with the polarization parallel to the director axis gives a much stronger signal than does the beam with the perpendicular polarization. The ⊥-signals rise exponentially with the time constant that is sensitive to the temperature and then stay constant in this time window. Each ∥-signal appears to have two components. As we will discuss the details of the two components in the later section, only a brief description is given here. One of the two components behaves just as the corresponding ⊥-signal. When the tails of the ∥- and the ⊥-signals are matched by multiplying the ⊥-signal by the number given in Figure 2, the additional component of the ∥-signal becomes apparent. The additional component of the ∥-signal rises instantaneously within the time resolution of the experiment (ca. 20 ns) and decays in about 10 $\mu$s. The ratio of the common rising component of the ∥-signal and the ⊥-signal reduces from 12 to 4.5 as the temperature increases from 25.0 to 46.0 °C. When the temperature rises above $T_{ni}$ (46.5 °C) by even less than 1 °C, the signal intensity decreases by nearly 3 orders of magnitude and the anisotropic diffraction efficiency disappears.

The longer time behavior of the signals is shown in Figure 3. All experimental conditions except the data acquisition are identical to those of Figure 2. Figure 3 represents how the common rising component in Figure 2 evolves in the longer time scale. In Figure 3, only the ∥-signals are shown. The shape of each ⊥-signal is similar to that of the corresponding ∥-signal, and the relative intensities of the ∥- and the ⊥-signals are similar to the multiplication numbers of Figure 2. The signals of Figure 3 decay following two complicated exponential functions plus a small background. An example of such components for the best fit of the ∥-signal is shown in Figure 3b. The small background component can be resolved better in a much longer time window and under milder excitation conditions (lower repetition rate and laser power). Therefore, if the first component that rises instantaneously and decays in microseconds, the additional component in the ∥-signal in Figure 2, is included, a total of four components are identified in the TG dynamics. We shall call these components the first, the second, the third, and the fourth component of the TG dynamics in the order of increasing time scale. When the temperature is increased, the intensities of the second component dominant in the submilliseconds, vary relatively little but the third component grows and becomes dominant near $T_{ni}$. Above $T_{ni}$, no diffraction signals in this time window are detectable.

## Discussion

Theoretical generalization of the nonlinear optical process of transient grating experiments has been worked out for off-resonant transient birefringence experiments.[15] On the other hand, the present experimental field configuration contains a resonant pump field and an off-resonant probe field. Therefore, this type of experiment is a hybrid transient grating experiment. Its theoretical generalization based on density matrix formalism is presented in the Appendix. It justifies that the TG signal is proportional to the square of the tensorial response function, that is

$$I(t) \propto |\tilde{\tilde{X}}(t)|^2 \qquad (2)$$

We assume that the physical origins responsible for the four components found in our diffraction signal are not correlated with one another. Under this assumption, the response function can be approximately written as a sum of four response functions representing each component, that is,

$$\tilde{\tilde{X}}(t) = \tilde{\tilde{X}}_1(t) + \tilde{\tilde{X}}_2(t) + \tilde{\tilde{X}}_3(t) + \tilde{\tilde{X}}_4(t) \qquad (3)$$

where $\tilde{\tilde{X}}_1(t)$ is the fastest component, $\tilde{\tilde{X}}_4(t)$ is the slowest, and so on. Since the time scales of the four contributions are notably different from one another, eq 3 should be acceptable. To fit the experimental data, we use the following functions for each response function

$$X_1(t) = A_1 \exp(-t/\tau_{d1}) \qquad (4)$$

$$X_2(t) = A_2[1 - \exp(-t/\tau_{r2})] \exp(-t/\tau_{d2}) \qquad (5)$$

$$X_3(t) = A_3[1 - \exp(-t/\tau_{r3})] \exp(-t/\tau_{d3}) \qquad (6)$$

$$X_4(t) = A_4 \exp(-t/\tau_{d4}) \qquad (7)$$

where $A$'s are the corresponding amplitudes and $\tau_r$ and $\tau_d$ denote the rise and the decay time constants. Theoretical details of the response function, the time constants, and the characteristics of the TG dynamics of this work are discussed in the Appendix. The first and the fourth components are assumed to be fully diffusive so that a usual diffusion equation such as the Smoluchowski equation could be used to obtain the response function. This is the limiting case of the overdamped motion of the Brownian oscillator. In contrast, we find that the second and the third components should be treated as the overdamped oscillator, since both of these contributions exhibit the rise-and-decay pattern as seen in Figures 2 and 3. These observations are clear evidence that there exist large inertial motions in the dynamical evolutions of these two components. Now we present a detailed discussion on the dynamical origin of each component.

**A. Fast Dynamics; $0 \leq t \leq \tau_{d1}$.** We first consider the dynamics in the short-time region (Figure 2). The ⊥-signals can be fitted with a single rising exponential function, while fitting the ∥-signals needs an additional decaying function. The common rising exponential function must be the rise part of $X_2(t)$ or $X_3(t)$. We take the limit that $X_2(t)$ is the dominant contribution for the common rising exponential, since only one exponential time constant is needed to fit the common rising background and obviously $\tau_{r3} \gg \tau_{r2}$ in the signals of Figure 3 at temperatures higher than 38 °C. Therefore, we use $X_1(t)$ and $X_2(t)$ to fit the ∥-signals and $X_2(t)$ alone to fit the ⊥-signals. In
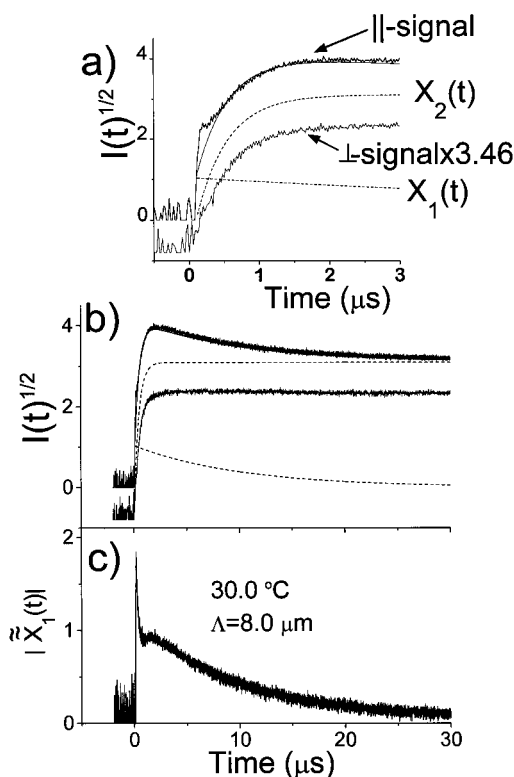
**Figure 4.** (a, b) Roots of the ∥-signal and the ⊥-signal are shown with $X_1(t)$, $X_2(t)$ (dashed curves), and $X_1(t) + X_2(t)$ (solid smooth curve). The ⊥-signal is shown downshifted for clarification. (c) The tailing background component $X_2(t)$ is subtracted from the root of the ∥-signal to give $|\tilde{\tilde{X}}(t)|$. The data of these plots are for 30.0 °C when $\Lambda = 8.0$ $\mu$m. The ordinates are in arbitrary experimental scale.

Figure 4 parts a and b, the best fit (solid smooth curve) to a ∥-signal (30.0 °C, $\Lambda = 8.0$ $\mu$m) and its components ($X_1(t)$, $X_2(t)$, dashed curves) are shown. The corresponding ⊥-signal is also shown. The fit is reasonably good except in the time region shorter than 0.5 $\mu$s. Assuming both the ∥- and the ⊥-signals have the common $X_2(t)$, the additional component is obtained by subtracting $X_2(t)$ from $(I_\parallel(t))^{1/2}$. It should correspond to $|\tilde{\tilde{X}}_1(t)|$ according to our classification. An example of $|\tilde{\tilde{X}}_1(t)|$ is shown in Figure 4c. It consists of an initial peak decaying in a few tens of nanoseconds followed by a single-exponential decay of 10 $\mu$s.

The physical origin of $|\tilde{\tilde{X}}_1(t)|$ that appears only in the ∥-signals needs to be explained. Such a complete anisotropic diffraction is rarely observed and is possible only when the polarizability change by photoexcitation responsible for the diffraction is highly parallel to the $z$-axis. For a possible origin of such a parallel polarization change, let us first assume that a photoinduced transient that has absorption at 633 nm may be produced with its transition dipole moment parallel to the $z$-axis. Its contribution to the ∥-signal might be made by the $\Delta k$ term in eq 1, and the decay time should represent the lifetime of the transient. We rule out the rotation of the transient for the observed decay of $|\tilde{\tilde{X}}_1(t)|$, since the rotation must induce the rise of the ⊥-signal at the same time with the decay of the ∥-signal. When the observed dynamics of $|\tilde{\tilde{X}}_1(t)|$ is decomposed into two components, the slower component that decays by 10 $\mu$s cannot be assigned to the lifetime decay of the photoinduced transient, since the decay time is insensitive to the temperature and is proportional to $\Lambda^2$ (Figure 5). The assignment of the faster component to the lifetime decay of the photoinduced transient does not gain much support, considering
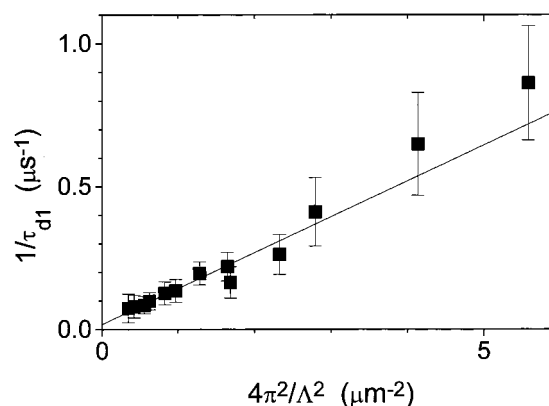


**Figure 5.** Plot of $1/\tau_{d1}$ versus $(4\pi^2)/\Lambda^2$. The error bars represent the fit uncertainties coming from the choice of fitting range.

the following: to our knowledge, the photoinduced transient of MBBA in this time scale has never been reported, and the faster decaying component is not observed for the isotropic sample at 47.0 °C.

Even though two components appear to be present in $|\tilde{\tilde{X}}_1(t)|$, they show the same dependence on the probe polarization. Therefore, we explain the shape with the picture of a single origin of thermal grating. We will explain first the dynamics of the thermal grating in our experimental conditions and will justify later its anisotropic behavior. Since our excitation wavelength is in the strong absorption region, the initial grating can be produced near the front surface of the sample. According to Urbach et al.,[6] the absorption depth is estimated to be the first few micrometers at 350 nm. Polarized UV spectra of nematic MBBA that we obtained indicate that the absorption depth at 355 nm is between 2 and 20 $\mu$m, which is close to the fringe spacing in the experiment. Therefore, a large temperature gradient in the direction normal to the glass surface ($y$-axis in Figure 1) is produced. Under this circumstance, the heat transfer to the front glass effectively diminishes the thermal grating. (The thermal conductivity of glasses is larger by 1 or 2 orders of magnitude than that of liquid crystals; therefore, the glass can work as an effective heat sink for the liquid crystal.) The initial fast decay in $|\tilde{\tilde{X}}_1(t)|$ is likely the thermal grating decay due to the interfacial heat-transfer process. After the fast interfacial heat transfer and the fast heat propagation into the bulk, the thermal gradient along $y$ reduces and thermal grating decays by diffusion as in the bulk, as is reflected in the single-exponential (after ∼1 $\mu$s) behavior of Figure 4.

We used the diffusional function of eq 4 to fit $|\tilde{\tilde{X}}_1(t)|$ after 1 $\mu$s and investigated the fringe spacing dependence of the decay time constant $\tau_{d1}$. When $1/\tau_{d1}$ is plotted versus $(4\pi^2)/\Lambda^2$ (Figure 5), a straight line with a negligible intercept is obtained. Its slope gives the thermal diffusion constant $D_{th} = (12.6 \pm 1.1)$ $\times 10^{-4}$ cm$^2$ s$^{-1}$. This value is somewhat larger than the thermal diffusion coefficient calculated from thermal properties of nematic MBBA,[16,17] $(8.3-10.5) \times 10^{-4}$ cm$^2$ s$^{-1}$.

In the isotropic phase of MBBA, the intensity of the TG signal is reduced by nearly 3 orders of magnitude and the anisotropic dependence of the probe polarization is removed. Only the first component is observed both in the ∥- and the ⊥-signals. As shown in Figure 2 for 47.0 °C, both signals decay nonexponentially. The decay pattern is similar to that shown in ref 18, where it is assigned to the interfacial heat transfer to the glass in addition to the usual thermal diffusion for the surface-sensitive TG method for the isotropic liquid crystal with the excitation wavelength in the strong absorption region. In this case, the

Dynamics of Nematic MBBA Film

*J. Phys. Chem. B, Vol. 102, No. 40, 1998* **7709**

thermal grating decay is described better by a numerical solution of the diffusion equation with the new boundary condition[18] than by the analytical exponential function. Instead, we use a trial function of the square of the biexponential function to fit the 47.0 °C signals of Figure 2. The two time constants, $1.3 \pm 0.2$ and $16.4 \pm 2.7$ $\mu$s, fit the decays reasonably well. When the fringe spacing dependence is investigated, the longer time constant is found to be proportional to $\Lambda^2$ and gives the diffusion constant of $(9.8 \pm 2.1) \times 10^{-4}$ cm$^2$ s$^{-1}$.

In the nematic phase of MBBA, the change of the refractive index due to the thermal fluctuation can be given by three terms as[11,19]

$$\Delta n^{\mathrm{th}} = \delta n_T^{\mathrm{th}} + \delta n_\rho^{\mathrm{th}} + \delta n_S^{\mathrm{th}}$$

$$= \left\{ \left(\frac{\partial n}{\partial T}\right)_\rho + \left(\frac{\partial n}{\partial \rho}\right)_T \left(\frac{\partial \rho}{\partial T}\right) + \left(\frac{\partial n}{\partial S}\right)_\rho \left(\frac{\partial S}{\partial T}\right) \right\} \delta T \quad (8)$$

where $\delta n_T^{\mathrm{th}}$ $(= (\partial n/\partial T)_\rho \delta T)$ represents the pure temperature grating and is probably negligible. $\delta T$ is the local temperature fluctuation. $\delta n_\rho^{\mathrm{th}}$ $(= (\partial n/\partial \rho)_T (\partial \rho/\partial T) \delta T)$ and $\delta n_S^{\mathrm{th}}$ $(= (\partial n/\partial S)_\rho (\partial S/\partial T) \delta T)$ represent gratings due to the temperature-induced density fluctuation and the temperature-induced order fluctuation, respectively. The density grating forms in an oscillatory fashion during the early thermalization process (not resolved in our time resolution) and decays by the relaxation of $\delta T$. In eq 8, as $(\partial n/\partial \rho)_T > 0$ and $\partial \rho/\partial T < 0$ are expected, $\delta n_\rho^{\mathrm{th}}$ is likely negative for both probe polarizations. The transient grating associated with the thermal-fluctuation-induced reordering is formed, since the thermalization reduces the order parameter in the bright region of the spatial grating. The ratio of the reordering gratings for the two probe polarizations is approximately equal to the ratio of the anisotropic part of molecular polarizability, that is,

$$\frac{(\delta n_S^{\mathrm{th}})_\|}{(\delta n_S^{\mathrm{th}})_\perp} \cong \frac{\alpha_\|^{\mathrm{aniso}}}{\alpha_\perp^{\mathrm{aniso}}} \quad (9)$$

This ratio is about $-2$ for a cylindrical shape molecule. $(\delta n_S^{\mathrm{th}})_\|$ should be positive, and $(\delta n_S^{\mathrm{th}})_\perp$ is negative.[11,20] Therefore, the two contributions from $\delta n_\rho^{\mathrm{th}}$ and $\delta n_S^{\mathrm{th}}$ are additive in the measurement of the ||-signal and subtractive in the ⊥-signal. With this picture, Terazima[11] explained his experimental results with the fact that the $I_\|^{\mathrm{th}}/I_\perp^{\mathrm{th}}$ is close to $(-7)^2$ near $T_{\mathrm{sn}}$, since the two contributions cancel each other in the ⊥-signal, and close to $(-2)^2$ near $T_{\mathrm{ni}}$, as the reordering grating becomes dominant at high nematic temperatures. However, the above model given in eq 8 does not support our TG decays. The common rising component in Figure 2 approaches the anisotropy ratio $(-2)^2$ of the temperature induced reordering grating as the temperature is increased, whereas Figure 2 shows that the first component has larger anisotropy ratios than $(-2)^2$ at the high nematic temperatures. Therefore, it is necessary to modify the model. First of all, we assume that the time scales of $\delta n_\rho^{\mathrm{th}}$ and $\delta n_S^{\mathrm{th}}$ are different and the two fluctuations are not correlated with each other. While $\delta n_\rho^{\mathrm{th}}$ follows the dynamics of $\delta T$ in our experimental time scale, $\delta n_S^{\mathrm{th}}$ may not. In fact, the delayed response of the reordering process upon the temperature perturbation has been found in several works[8-10] of liquid crystals. This is the manifestation of the inertial behavior.

The appropriate changes of refractive indices for the parallel and the perpendicular waves to the director axis are related to the components of the third-order nonlinear susceptibility tensor $\tilde{\tilde{X}}$ as[4]

$$\Delta n_\| = \frac{2\pi(\chi_{xzzz} + \chi_{zzzz})}{n_\|} |\mathbf{E}_{\mathrm{pu}}|^2$$

$$\Delta n_\perp = \frac{2\pi(\chi_{xxzz} + \chi_{zxzz})}{n_\perp} |\mathbf{E}_{\mathrm{pu}}|^2 \quad (10)$$

where the indices of $\chi$ are defined in the order of the directions of the diffraction field, the probe field ($\mathbf{E}_{\mathrm{pr}}$), and the two pump fields ($\mathbf{E}_{\mathrm{pu}}$). When a molecule like MBBA whose shape is highly ellipsoidal is preferentially aligned along the director axis and the electronic excitation is produced along the director axis, the initial induced fluctuating polarizability is likely highly anisotropic. That is, $\chi_{zzzz}(0) \gg (\chi_{xzzz}(0), \chi_{zxzz}(0)) \gg \chi_{xxzz}(0)$ and $\Delta n_\|(0) \gg \Delta n_\perp(0)$. In this case, $\mathbf{E}_{\mathrm{pr}}$ polarized parallel to the director axis is preferentially scattered strongly, whereas $\mathbf{E}_{\mathrm{pr}}$ polarized perpendicular to the director axis is less strongly scattered. The initial anisotropy of the polarizable ellipsoid should decrease with the temperature as the initial order parameter is reduced and is zero in the isotropic phase. When the thermal grating is induced by the temperature-induced density change alone, the initial order parameter is not affected and, therefore, a large initial anisotropic polarizability change is created. Especially, considering the molecules near the surface can align better, the big initial anisotropy in Figure 2 is possible. This is reflected in the probe polarization dependence of the diffraction signals in Figure 2. The difference of the two diffraction intensities at zero time is large at low nematic temperatures but is small at high nematic temperatures. In the isotropic phase, the polarizability change tensor should be isotropic with small amplitude, as molecules reorient fast, and should produce equal and weak intensities of diffraction for the two polarizations. The initial anisotropy of the polarizability change relaxes by the density relaxation and by the disordering process in the bright region of the grating. The two processes are in-phase in the ||-signal and out-of-phase with a negligible thermal component in the ⊥-signal, and they follow different dynamics. This dynamical separation of the two components was not identified in the work of Terazima[11] under the weak absorption condition. Under our strong absorption condition, the temperature jump is much larger because of shorter absorption depth and more absorbed photons and the adjustment by disordering needs a delayed time.

Under this scheme, we can assign the dynamics observed in the short time scale; the first component is assigned to the transient grating associated with the density grating induced by the temperature perturbation, and the second component represents the reordering grating induced by the temperature perturbation. The anisotropy ratio of probe polarization dependency of the second component is higher than $(-2)^2$ at low nematic temperatures, since the molecules are more associated, but it approaches the expected ratio based on the molecular picture in eq 9 as the temperature is increased.

**B. Intermediate Dynamics; $\tau_{\mathrm{d1}} \leq t \leq \tau_{\mathrm{d3}}$.** In the submilliseconds to milliseconds, the second and third components dominate the TG dynamics. These two components are in general described by the exponential rise followed by the exponential decay as in eqs 5 and 6. The rise times of the second component are determined from the signals in Figure 2, and they vary substantially with the temperatures between 170 ns at 25 °C and 2.8 $\mu$s at 44 °C at $\Lambda = 8.0$ $\mu$m. The second component undergoes the decay dynamics shown in Figure 3.

**TABLE 1: Fit Parameters for Eqs 4−7[a]**

| T (°C) | probe polarization | 1st component τ$_{d1}$ (μs) | 2nd component | | | 3rd component | | | 4th component | |
|---|---|---|---|---|---|---|---|---|---|---|
| | | | A$_2$ | τ$_{r2}$ | τ$_{d2}$ (ms) | A$_3$ | τ$_{r3}$ (ms) | τ$_{d3}$ (ms) | A$_4$ | τ$_{d4}$ (ms) |
| 25.0 | ‖ | 12 | 2.6 | 170 ns | 0.29 | 1.3 | ∗ | 5.1 | 0.18 | 118 |
| | ⊥ | | 0.88 | 170 ns | 0.31 | 0.29 | ∗ | 6.2 | 0.14 | ? |
| 30.0 | ‖ | 10 | 3.3 | 600 ns | 0.37 | 1.6 | ∗ | 5.5 | 0.67 | 75 |
| | ⊥ | | 0.99 | 600 ns | 0.36 | 0.33 | ∗ | 6.1 | 0.44 | ? |
| 34.0 | ‖ | 9.2 | 2.0 | 670 ns | 0.31 | 2.2 | ∗ | 5.0 | 0.62 | ? |
| | ⊥ | | 0.75 | 610 ns | 0.42 | 0.48 | ∗ | 5.0 | 0.40 | ? |
| 38.0 | ‖ | 9.2 | 4.2 | 1.7 μs | 0.80 | 4.6 | 2.4 | 8.9 | 0.36 | ? |
| | ⊥ | | 2.1 | 1.2 μs | 0.76 | 2.8 | 2.3 | 7.0 | 0.64 | ? |
| 41.0 | ‖ | 7.1 | 6.2 | 2.1 μs | 1.3 | 22 | 10 | 9.6 | 0.28 | ? |
| | ⊥ | | 2.5 | 2.0 μs | 1.2 | 11 | 13 | 8.1 | 0.40 | ? |
| 44.0 | ‖ | ? | 6.0 | 2.8 μs | 0.83 | 11 | 3.6 | 15 | 0.02 | ? |
| | ⊥ | | 2.3 | 2.0 μs | 0.78 | 3.2 | 2.7 | 14 | 0 | ? |
| 46.0 | ‖ | ? | 3.6 | 2.0 μs | 0.14 | 24 | 16 | 22 | | |
| | ⊥ | | 1.7 | 2.0 μs | 0.24 | 17 | 23 | 15 | | |

[a] A's are in arbitrary experimental units. τ$_{d1}$'s and τ$_{r2}$'s are determined from the signals of Figure 2. τ$_{d4}$'s are determined from separate experiments under the milder excitation conditions and in the longer time window. The other fit parameters are determined from the ‖-signals of Figure 3 and the corresponding ⊥-signals. A$_4$'s represent the background amplitudes in the signals of Figure 3. Some τ$_{d1}$'s and τ$_{d4}$'s (denoted with ?) were not determined as the relative intensities of the corresponding components are too small. Some τ$_{r3}$'s (denoted with ∗) were not determined but must be longer than the corresponding τ$_{r2}$. The fit qualities of the signals at 46.0 °C are not excellent. We do not list A$_1$ values because data of Figures 2 and 3 are obtained under the different acquisition conditions and the attempts to rescale them may result in misleading.

The third component of the TG dynamics is the one whose amplitude increases with the temperature as shown in Figure 3. In Figure 3b, examples of the fitting components $X_2(t)$ and $X_3(t)$ and the background $X_4(t)$ are shown. The fit parameters using eqs 4−7 are summarized in Table 1.

The rise followed by decay of the second component can be considered as the disordering process induced by the temperature perturbation followed by recovery of ordering in the bright region of the grating. The temperature perturbation, whose temporal behavior is determined by the pump pulse time profile, imposes a δ-function force on the nematic-ordered system and eventually lowers the order parameter temporally. This process appears as the rise pattern in the signal. Then, the disordered nonequilibrium state relaxes to the initial equilibrium state, which is a rather ordered configuration. The rise of the second component due to the disordering should be faster than the decay due to the ordering because the former is induced by a sudden temperature perturbation, while the latter is induced by an internal stabilization process.

The third component of the TG dynamics is enormously affected by the temperature. Pinkevich et al.[4] showed theoretically that the large optical nonlinearity near the transition temperature can be produced from phototransformed states. That is, the third component might be considered as the disorder−order process induced by the phototransformer. This process is slower than the disorder−order process induced by the temperature perturbation, and the photoisomerized *cis*-MBBA could be a candidate for the phototransformer. However, we cannot rule out the possibility of the photoinduced melted state of the liquid crystal for the phototransformer. Investigation of the nonisomerizing liquid crystals may be helpful for the clear answer. For MBBA, we investigated the dependence on the irradiance of the excitation (Figure 6). The effect of the photoisomer is expected to be linear with the laser power, while that of the photoinduced melted state is not. At 40 °C, below the irradiancce of 3.2 mJ/cm², the second and the third components are not clearly separated. At 10 mJ/cm², the third component shows up with an abruptly increasing rise time. The two components do not change much between 10 and 20 mJ/cm². Above this irradiance, both components gradually drop their amplitudes, probably because of some laser-induced instabilities. Overall, the integrated area of the second component is relatively invariant with the irradiance up to 25 mJ/
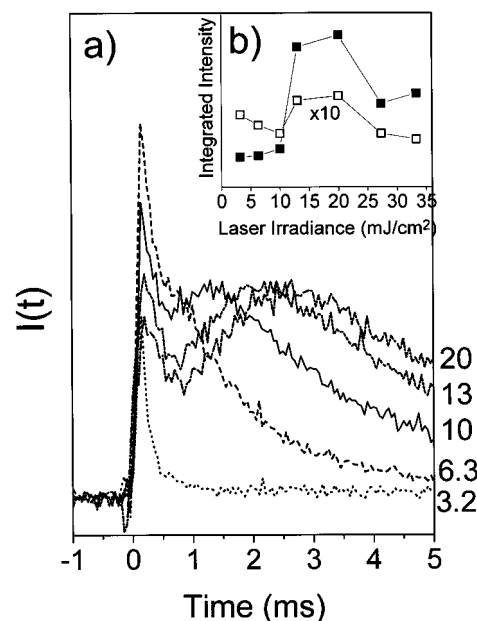


**Figure 6.** (a) Effect of laser irradiance on the second and the third components when the temperature is 40 °C. The grating spacing is 8.0 μm. The numbers on the right are the laser irradiances in the unit of mJ/cm². The inserted figure (b) shows the integrated intensities of the second (□, $10 \times A_2\tau_{d2}^2/(\tau_{r2} + \tau_{d2})$) and the third (■, $A_3\tau_{d3}^2/(\tau_{r3} + \tau_{d3})$) components as a function of the laser irradiance.

cm², while the area of the third component has a breakup irradiance of ∼10 mJ/cm².

The breakup development of the third component strongly suggests the photoinduced melting process for the major cause of the third component. At 40 °C, the power density needed for the temperature jump to reach the isotropic phase is calculated to be ∼13 J/cm³ from a known heat capacity.[21] In the irradiance dependence of the third component at 40 °C, the breakup irradiance for the development of the third component, 10 mJ/cm², gives the power density 10 J/cm³, assuming an absorption depth of 5 μm; this is close to the one calculated with the heat capacity. The difference may be due to an inaccurate estimate of the absorption depth and an ignorance of the heat transfer to the front glass. Our experimental irradiance of 10 mJ/cm² would result in significant local melting
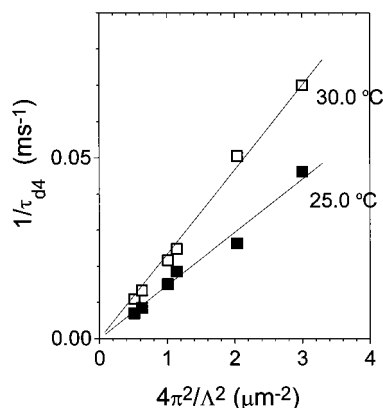
**Figure 7.** Plot of $1/\tau_{d4}$ versus $(4\pi^2)/\Lambda^2$ at 25 and 30 °C. Each straight line is the best linear least-squares fit.

when the temperature is higher than 40 °C. The increasing trend of the rise and the decay time constants of the two components also has the break near this temperature. This behavior may imply that weaker intermolecular interactions at higher nematic temperatures reduce the inertia for reordering. Above this temperature, the rise time halts increasing and the decay time decreases slightly as the photoinduced melting process becomes significant. The photoinduced melting process affects the second component merely as the temperature jump is produced near the surface. As the melting propagates into the bulk, it changes the nature of the phototransformer in the bulk.

At high nematic temperatures, higher (up to the fourth) order diffractions are visible. While the details in the dynamics of the multiple order diffractions will be written in another paper,[22] we only mention the implication of it with relevance to this paper. The multiple order diffractions imply that the spatial shape of the grating evolves out of sinusoidality. We found that the high order diffractions have much stronger dynamic features in the milliseconds than in the submilliseconds. This may imply that the third component is more responsible for the dynamic distortion of the spatial grating. Possibly, the laser-induced melting caused the propagation of the ordering (or disordering) torque along the $x$-axis and the distortion of the spatial grating.

**C. Slow Dynamics; $\tau_{d3} \leq t$.** The slowest dynamics, corresponding to the fourth component, decays exponentially, and its decay time constant $\tau_{d4}$ is found to be directly proportional to $\Lambda^2/(4\pi^2)$ as shown in Figure 7. The linearity indicates that the fourth component is related to a pure diffusional motion. From the slopes of the plots in Figure 7, we obtain diffusion coefficients of $1.86 \times 10^{-7}$ cm$^2$ s$^{-1}$ at 25 °C and $2.35 \times 10^{-7}$ cm$^2$ s$^{-1}$ at 30 °C. These values are comparable to the reported[6] value of the mass diffusion coefficient along the direction normal to the director axis of MBBA at 22 °C, $D_\perp = 1.61 \times 10^{-7}$ cm$^2$ s$^{-1}$. These values at three different temperatures can be used to estimate the activation energy of the mass diffusion by using the Arrhenius analysis, $E_a^\perp = 35.2$ kJ/mol, which is in excellent agreement with the reported values.[12,23] The origin of this fourth component is therefore the mass diffusion of photogenerated *cis*-MBBA via modifications of the density and the alignment of the liquid crystal.[12] Therefore, its effect on the transient grating should be much larger in the nematic phase than in the isotropic phase. While the formation of *cis*-MBBA is believed to take place within the excitation pulse, the development of the density and disordering fluctuaction induced by the photoisomer may wait some time. However, the rise part of $X_4(t)$ is buried under much stronger intensities of the other components. Since the

amplitude of $X_4(t)$ is too small, the ignorance of the rise part of $X_4(t)$ will not affect the interpretation of the other components.

**Conclusions**

Some large anisotropic molecules forming liquid crystal phases have huge nonlinear optical properties. The anisotropic alignment in liquid crystal phases enhances greatly the nonlinear optical properties of the system. The TG method, a version of the four-wave mixing technique, is effective for the study of various dynamics of anisotropic liquid crystal systems. In this work, we have applied the TG method for the investigation of many interesting properties of nematic MBBA, including nonlinear optical properties and diffusion. MBBA has strong absorption at the excitation wavelength of 355 nm and no absorption at the probe wavelength of 632 nm; that is, the experimental configuration of the resonant pump field and off-resonant probe field corresponds to a hybrid transient grating. Complicated features of the dynamics of nematic MBBA have been understood from the probe polarization dependence of the TG signal.

Under the strong absorption condition, the TG signals from nematic MBBA exhibit many nonlinear and anisotropic components in the time scale of microseconds to milliseconds. The dynamics are explained in terms of the overdamped motions of the Brownian oscillator, which show the rise-and-decay patterns. The temperature perturbation induces the density grating and the reordering grating. The anisotropic alignment of the nematic phase produces the highly anisotropic density grating, and the probe polarization dependence of the reordering grating decreases with the temperature as the order parameter of the nematic phase decreases. The large optical nonlinearity of the melted state of nematic MBBA, which increases greatly as the temperature approaches $T_{ni}$, gives another component of the signal due to the disorder−order process. Mass diffusion of the photoisomerized MBBA appears as the slowest component of the TG signal decay. When MBBA is heated above $T_{ni}$, only very weak thermal grating is observed.

**Appendix**

The molecular density matrix, for a two-electronic level system with a ground-state g and an excited state e at **r**, is in general written as

$$\rho(\mathbf{r},t) = \sum_{\alpha,\beta=g,e} |\alpha\rangle \rho_{\alpha\beta}(\mathbf{r},t) \langle\beta| \qquad (A1)$$

where $\rho_{\alpha\beta}(\mathbf{r},t)$ are density operators in the molecular nuclear space. The diagonal density operators describe the nuclear dynamics of either the ground or excited state, whereas the off-diagonal density operators describe the evolution of the electronic coherence states. In this work, the external field consists of two resonant pump fields and a single off-resonant probe field. Therefore, the total external field is given as

$$\mathbf{E}(\mathbf{r},t) = \mathbf{E}_{pu}(\mathbf{r},t) + \mathbf{E}_{pr}(\mathbf{r},t) \qquad (A2)$$

where the pump and probe fields are, respectively,

$$\mathbf{E}_{pu}(\mathbf{r},t) = \mathbf{E}_{pu}(t) \exp(i\mathbf{k}_1\cdot\mathbf{r} - i\omega_{pu}t) +$$
$$\mathbf{E}_{pu}(t) \exp(i\mathbf{k}_2\cdot\mathbf{r} - i\omega_{pu}t) + \text{c.c.}$$

$$\mathbf{E}_{pr}(\mathbf{r},t) = \mathbf{E}_{pr}(t - t_d) \exp(i\mathbf{k}_3\cdot\mathbf{r} - i\omega_{pr}t) + \text{c.c.} \quad (A3)$$

In eq A3, $\mathbf{E}_{pu}(t)$ and $\mathbf{E}_{pr}(t)$ denote the time profiles of the pump

and the probe field amplitudes and $\omega_{pu}$ and $\omega_{pr}$ are the frequencies of the resonant pump and the off-resonant probe fields, respectively. c.c. denotes the complex conjugate. $t_d$ is the experimental sampling time, although we use a continuous wave for the probe field. Since the time scale of detection is much shorter than the time scales of the relevant dynamics, it is safe to assume that the probe beam is a pulse.

Assuming that the optical processes are sequential, we consider the creation of the transient grating by the second-order interaction with the pump fields. The evolution of the composite system is determined by the quantum Liouville equation

$$\frac{d}{dt}\rho(\mathbf{r},t) = -\frac{i}{\hbar}[H - \mathbf{E}_{pu}(\mathbf{r},t)\cdot\mathbf{V},\rho(\mathbf{r},t)] \qquad (A4)$$

where the material Hamiltonian and the electric dipole operator are denoted as $H$ and $\mathbf{V}$, respectively,

$$H = |g\rangle H_g \langle g| + |e\rangle(H_e + \omega_{eg})\langle e|$$

$$\mathbf{V} = \hat{\mu}(|g\rangle\langle e| + |e\rangle\langle g|) \qquad (A5)$$

The nuclear Hamiltonians of the ground and the excited states are denoted as $H_g$ and $H_e$, respectively. $\hat{\mu}$ is the electric dipole matrix element.

By following the procedure presented in ref 15, the generalized master equation for the ground-state density matrix that describes the creation of the transient grating is obtained as

$$\frac{d}{dt}\rho_{gg}(\mathbf{r},t) = -iL_{gg}\rho_{gg}(\mathbf{r},t) - i|\mathbf{E}_{pu}(t)|^2\,\hat{e}_1\hat{e}_2:[A_R\hat{\mu}\hat{\mu},\rho_{gg}(\mathbf{r},t)] +$$
$$|\mathbf{E}_{pu}(t)|^2\hat{e}_1\hat{e}_2:[A_I\hat{\mu}\hat{\mu},\rho_{gg}] - 2|\mathbf{E}_{pu}(t)|^2\hat{e}_1\hat{e}_2:\ A_I\hat{\mu}\rho_{ee}\hat{\mu} \quad (A6)$$

where $\hat{e}_1$ and $\hat{e}_2$ are the unit vectors of the two pump fields. $A_R$ and $A_I$ are the real and imaginary parts of an auxiliary function $A(\mathbf{r},\Omega)$, which is defined as

$$A(\mathbf{r},\Omega) \equiv \frac{\exp\{-i(\mathbf{k}_1 - \mathbf{k}_2)\cdot\mathbf{r}\}}{\omega_{pu} - \omega_{eg} + i\Gamma} \qquad (A7)$$

where $\Gamma$ is the electronic dephasing constant. The rotating wave approximation was invoked to obtain eq A6. $L_{gg}$ is the commutator defined as, for an arbitrary operator $A$,

$$L_{gg}A \equiv (H_gA - AH_g)/\hbar \qquad (A8)$$

In eq A6, the first term represents the dynamical evolution of the ground state nuclear degrees of freedom. The second term corresponds to the transient birefringence contribution, whereas the third term describes the transition from the ground state to the excited state by the interaction with the pump fields. Likewise, the final term is associated with the transition from the excited state to the ground state. Note that the transition rate is proportional to the imaginary part of $A(\mathbf{r},\Omega)$, whereas the transient birefringence contribution is proportional to the real part of $A(\mathbf{r},\Omega)$.

Hereafter, we neglect the contributions from the third and fourth terms, since the lifetime of the electronic excited state is much shorter than that of the experimental time scale. From the definition of the third-order polarization

$$\mathbf{P}^{(3)}(\mathbf{r},t) = Tr[\hat{\mu}\{\rho_{eg}^{(3)}(\mathbf{r},t) + \rho_{ge}^{(3)}(\mathbf{r},t)\}] \qquad (A9)$$

and, considering the polarization component with a wave vector

of $\mathbf{k}_s = \mathbf{k}_1 - \mathbf{k}_2 + \mathbf{k}_3$, we find that the homodyne-detected fourth-rank tensorial signal is

$$\tilde{\tilde{I}}(t_d) = \int_{-\infty}^{\infty}dt\,\mathbf{P}^*(\mathbf{k}_s,t)\cdot\mathbf{P}(\mathbf{k}_s,t)$$

$$= \int_{-\infty}^{\infty}dt|\mathbf{E}_{pr}(t - t_d)|^2 \times |\int_0^{\infty}d\tau\,|\mathbf{E}_{pu}(t - \tau)|^2\tilde{\tilde{X}}(\tau)|^2 \quad (A10)$$

where the fourth-rank tensorial response function

$$\tilde{\tilde{X}}(\tau) \equiv \left\langle \frac{i}{\hbar}[\tilde{\alpha}_{off}(\omega_{pr},\,\tau),\,\tilde{\alpha}_{res}(\omega_{pu},0)]^{\otimes} \right\rangle \qquad (A11)$$

Here the off-resonant and the resonant polarizability tensor operators are denoted as $\tilde{\alpha}_{off}(\omega_{pr})$ and $\tilde{\alpha}_{res}(\omega_{pu})$, respectively. These are defined as

$$\tilde{\alpha}_{off}(\omega_{pr}) \equiv \frac{2\omega_{eg}\hat{\mu}\otimes\hat{\mu}}{\hbar(\omega_{eg}^2 - \omega_{pr}^2)}$$

$$\tilde{\alpha}_{res}(\omega_{pu}) \equiv \frac{\hat{\mu}\otimes\hat{\mu}}{\hbar(\omega_{pu} - \omega_{eg} + i\Gamma)} \qquad (A12)$$

$\tilde{\alpha}_{off}(\omega_{pr},\tau)$ is the Heisenberg representation of $\tilde{\alpha}_{off}(\omega_{pr})$. In eq A11, the commutator $[...]^{\otimes}$ is defined as, for two arbitrary operators $A$ and $B$, $[A,B]^{\otimes} = A\otimes B - B\otimes A$. Equation A10 with eqs A11 and A12 constitutes the principal results, which describes the transient grating signal for our experimental configuration.

Further simplification can be achieved by noting that the time scale of the measured dynamics is much slower than that of the pulse width so that we have the hybrid transient grating signal

$$I(t_d) = |\mathbf{E}_{pr}|^2|\mathbf{E}_{pu}|^4|\tilde{\tilde{X}}(t_d)|^2 \qquad (A13)$$

The experimental results are analyzed in terms of the response function given in eq A11.

In this work, we assume that the relevant nuclear degrees of freedom associated with the transient modulations of the refractive index of the nonlinear optical sample are determined by the corresponding Langevin equation

$$m\frac{d^2Q}{dt^2} + m\gamma\frac{dQ}{dt} + m\Omega^2Q = f(t) \qquad (A14)$$

where $m$, $\gamma$, and $\Omega$ denote the reduced mass, the damping constant, and the corresponding frequency of this oscillator. $f(t)$ represents the random fluctuating force whose autocorrelation function is related to the damping constant by the fluctuation−dissipation theorem. One can interpret that the coordinate $Q$ represents the collective variable modulating the refractive index. By Taylor expanding the two polarizabilities defined in eq A12 in terms of the collective coordinate $Q$,

$$\tilde{\alpha}_{off} = \tilde{\alpha}_{off,0} + \frac{\partial\tilde{\alpha}_{off}}{\partial Q}\Big|_0 Q + \dots$$

$$\tilde{\alpha}_{res} = \tilde{\alpha}_{res,0} + \frac{\partial\tilde{\alpha}_{res}}{\partial Q}\Big|_0 Q + \dots \qquad (A15)$$

and by taking into account the first-order expansion (Herzberg−

Dynamics of Nematic MBBA Film

*J. Phys. Chem. B, Vol. 102, No. 40, 1998* **7713**

Teller) terms, we find that the response function of this Brownian oscillator is

$$\tilde{\tilde{X}}(t) = \left(\frac{\partial \tilde{\alpha}_{off}}{\partial Q}\right)_0 \otimes \left(\frac{\partial \tilde{\alpha}_{res}}{\partial Q}\right)_0 \frac{1}{mW} \exp(-\gamma t/2) \sin Wt \qquad (A16)$$

where $W \equiv (\Omega^2 - \gamma^2/4)^{1/2}$. If the ratio $2\Omega/\gamma$ is smaller than unity, this Brownian oscillator is overdamped and the corresponding response function consists of two exponential functions as

$$\tilde{\tilde{X}}(t) = \left(\frac{\partial \tilde{\alpha}_{off}}{\partial Q}\right)_0 \otimes \left(\frac{\partial \tilde{\alpha}_{res}}{\partial Q}\right)_0 \frac{1}{2m\omega} \exp(-\gamma t/2) [\exp(\omega t) - \exp(-\omega t)] \quad (A17)$$

where $\omega \equiv (\gamma^2/4 - \Omega^2)^{1/2}$.

Equation A17 provides us with the motivation to use the function of rise-and-decay for the experimental data.

$$X(t) = A[1 - \exp(-t/\tau_r)] \exp(-t/\tau_d) \qquad (A18)$$

where the rise and the decay time constants are $\tau_r = 1/2\omega$ and $\tau_d = (\gamma/2 - \omega)^{-1}$, respectively.

In the highly overdamped limit ($\gamma/2 \gg \Omega$), where the diffusive equation such as the Smoluchowski equation is applicable, eq A17 or eq A18 can be approximated as

$$X(t) = A \exp(-t/\tau_d) \qquad (A19)$$

where the decay constant $\tau_d$ is $\Omega^2/\gamma$, which is related to the diffusion constant as $\tau_d = \Lambda^2/(4\pi^2 D)$. This approximated expression eq A19 is employed in the fittings of the first and fourth components in the signal (see eqs 4 and 7).

**References and Notes**

(1) (a) Khoo, I.-C. *Liquid Crystals*; John Wiley & Sons: New York, 1995. (b) Khoo, I.-C.; Wu, S.-T. *Optics and Nonlinear Optics of Liquid Crystals*; World Scientific: Singapore, 1993.

(2) de Gennes, P. G.; Prost, J. *The Physics of Liquid Crystals*, 2nd ed.; Clarendon Press: Oxford, 1993.

(3) Chandrasekhar, S. *Liquid Crystals*, 2nd ed.; Cambridge University Press: Cambridge, 1992.

(4) Pinkevich, I. P.; Reznikov, Yu. A.; Reshetnyak, V. Yu.; Yaroshchuk, O.V. *Int. J. Nonlinear Opt. Phys*. **1992**, *1*, 447.

(5) Odulov, S. G.; Reznikov, Yu. A.; Soskin, M. S.; Khizhnyak, A. I. *Sov. Phys. JETP* **1982**, *55*, 354.

(6) Urbach, W.; Hervet, H.; Rondelez, F. *J. Chem. Phys*. **1985**, *83*, 1877.

(7) Hsiung, H.; Shi, L. P.; Shen, Y. R. *Phys. Rev. A*. **1984**, *30*, 1453.

(8) (a) Khoo, I. C.; Normandin, R. *J. Appl. Phys*. **1984**, *55*, 1416. (b) Khoo, I. C.; Normandin, R. *IEEE J. Quantum Electron*. **1985**, *QE-21*, 329. (c) Khoo, I. C.; Lindquist, R. G.; Michael, R. R.; Mansfield, R. J.; LoPresti, P. *J. Appl. Phys*. **1991**, *69*, 3853.

(9) Khoo, I. C.; Shepard, S. *J. Appl. Phys*. **1983**, *54*, 5491.

(10) Eichler, H. J.; Macdonald, R. *Phys. Rev. Lett*. **1991**, *67*, 2666.

(11) Terazima, M. *Bull. Chem. Soc. Jpn*. **1996**, *69*, 1881.

(12) Ohta, K.; Terazima, M.; Hirota, N. *Bull. Chem. Soc. Jpn*. **1995**, *68*, 2809.

(13) Kim, S. H.; Kim, S. K. *Bull. Korean Chem. Soc*. **1996**, *17*, 365.

(14) Jin, D.; Kim, H.; Kim, S. H.; Kim, S. K. *J. Phys. Chem. B* **1997**, *101*, 10757.

(15) Cho, M.; Du, M.; Scherer, N. F.; Fleming, G. R.; Mukamel, S. *J. Chem. Phys*. **1993**, *99*, 2410.

(16) Kuss, E. *Mol. Cryst. Liq. Cryst*. **1978**, *47*, 71.

(17) Koren, G. *Phys. Rev. A* **1976**, *13*, 1177.

(18) Terazima, M.; Kojima, Y.; Hirota, N. *Chem. Phys. Lett*. **1996**, *259*, 451.

(19) Khoo, I. C. *IEEE J. Quantum Electron*. **1986**, *QE-22*, 1268.

(20) Palffy-Muhoray, P. *Liquid Crystals, Applications and Uses*; Bahadur, B., Ed.; World Scientific: Singapore, 1990; Vol. 1.

(21) Ostrovskii, B. I.; Taraskin, S. A.; Strukov, B. A.; Sonin, A. S. *Sov. Phys. JETP* **1977**, *44*, 363.

(22) Yoon, B.; Lee, I.; Kim, S. K.; Kim, H. *Bull. Korean Chem. Soc*., in preparation.

(23) Krüger, G. J. *Phys. Rep*. **1982**, *82*, 229.